EDGE ARTICLE

Check for updates

View Article Online
View Journal | View Issue

Chiral tether-guided selective synthesis of D_n-symmetric chiral conjugated nanorings

Tai An,†[ab] Jiayao Yao,†[d] Zuo Xiao, [ID] *[a] Qi Yu,[ab] Yu Wang,[a] Yueyue Gao,[f] Yixiao Song,[a] Zuoxin Huang,*[d] Zheng Ding,[a] Xinyue Zhang,[ab] Yuanpeng Xie, [ID] [e] Menglan Lv,*[e] Chuantian Zuo, [ID] *[a] Junqiao Ding [ID] [g] and Liming Ding [ID] *[c]

Chiral conjugated nanorings with D_n symmetry exhibit extraordinary circularly polarized luminescence (CPL) properties due to their unique cylindrical helical conjugated system. However, their synthesis faces challenges such as numerous atropisomers and tedious separation and chiral resolution processes, which severely hinder their development. In this work, we report a chiral tether-guided synthesis strategy. By introducing a strained planar chiral alkyl chain tether into the fused-ring building unit of the nanoring, the energy differences between the various atropisomers of the nanoring are significantly increased. This guides the formation of the thermodynamically most stable D_n-symmetric isomer during synthesis, thus greatly enhancing the selectivity. Four chiral nanorings, D_3-(P)-NR1, D_4-(P)-NR1, D_3-(M)-NR2, and D_4-(M)-NR2, as well as their enantiomers, were facilely obtained through this method. All molecules have shown remarkable and stable CPL capability, with a luminescence dissymmetry factor up to 0.076.

Introduction

In recent years, organic luminescent materials have achieved widespread applications in fields such as electroluminescence, biological probes, information encryption, sensing and detection.[1–7] Chirality further endows them with circularly polarized luminescence (CPL) properties, significantly expanding their application potential and making them highly promising for 3D displays, optical storage, polarized imaging, chiral sensing, and spintronics.[8–15] Two key metrics for evaluating the performance of chiral luminescent materials are the photoluminescence quantum yield (φ) and the luminescence dissymmetry factor (g_{lum}). For organic luminescent molecules, the φ can reach 100% through molecular design and excited-state modulation. However, the intrinsic g_{lum} values of most organic chiral molecules typically fall within the range of 10^{-5}

to 10^{-3},[16] far below the theoretical extremes (± 2). Developing organic chiral molecules with intrinsically large g_{lum} values holds significant scientific importance.

Theoretically, the g_{lum} of chiral luminescent molecules can be described by the following equation:

$$g = \frac{4|\mu_{ij}||m_{ij}|\cos\theta}{|\mu_{ij}|^2 + |m_{ij}|^2}$$

where μ_{ij} and m_{ij} represent the electric transition dipole moment and magnetic transition dipole moment, respectively, during the transition from excited state 'i' to ground state 'j', and θ is the angle between the two transition dipole moments.[17,18] Since the luminescence of most organic molecules follows Kasha's rule, the transition of interest is typically from the S_1 to S_0 state.[19] The equation indicates that to maximize the g value while maintaining high luminescence intensity, both μ and m must be large and comparable in magnitude, while their dipole moments must be aligned parallel or antiparallel (*i.e.*, $\theta = 0$ or 180). However, for most organic chiral molecules, m is much smaller than μ, making it difficult to enhance g_{lum}.[20] Therefore, the key to improving g_{lum} lies in molecular design strategies that enhance m while ensuring μ and m remain parallel or antiparallel. In recent years, significant efforts have been devoted to exploring chiral organic luminescent molecules with high g_{lum} values.[21–47] Among all reported chiral organic emitters, conjugated nanorings with D_n symmetry exhibit exceptionally high intrinsic g_{lum}. For example, Isobe's D_4-symmetric (*P*)-(12,8)-[4]CC[45] and Du's D_4-symmetric (+)-[4]CAn$_{2,6}$ ref. 46 achieved $|g_{lum}|$ of 0.152 and 0.103,

[a] Key Laboratory of Nanosystem and Hierarchical Fabrication (CAS), National Center for Nanoscience and Technology, Beijing 100190, China. E-mail: xiaoz@nanoctr.cn; zuocht@nanoctr.cn

[b] University of Chinese Academy of Sciences, Beijing 100049, China

[c] School of Chemical Engineering and Light Industry, Guangdong University of Technology, Guangzhou 510006, China. E-mail: ding@gdut.edu.cn

[d] Sinopec Research Institute of Petroleum Processing Co., Ltd, Beijing 100083, China. E-mail: huangzx@ripp.sinopec.com

[e] School of Chemistry and Chemical Engineering, Guizhou University, Guiyang 550025, China. E-mail: mllv@gzu.edu.cn

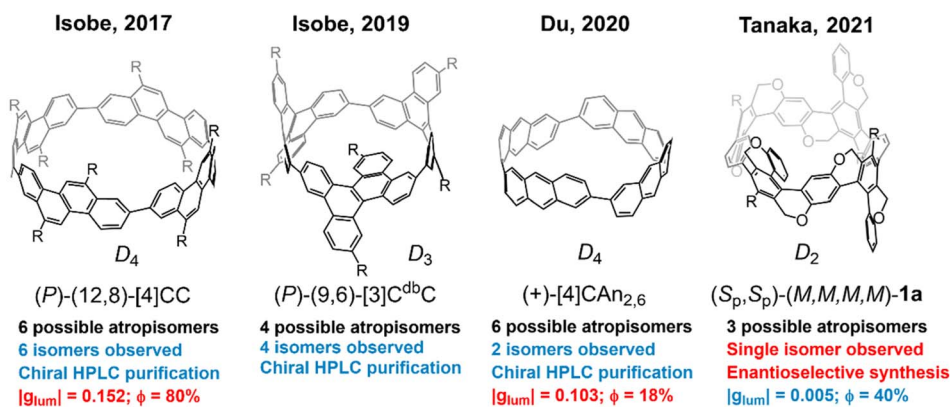[f] School of Future Technology, Henan University, Zhengzhou 450046, China

[g] School of Chemical Science and Technology, Yunnan University, Kunming 650091, China

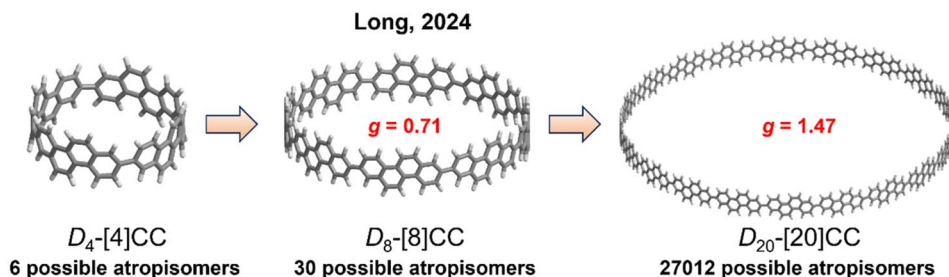† These authors contributed equally to this work.

respectively (Fig. 1a), representing the only two purely organic chiral emitters with $|g_{lum}|$ on the order of 10^{-1} at the molecular level. Notably, (P)-(12,8)-[4]CC also exhibited a high fluorescence quantum yield of 80%. The extraordinary $|g_{lum}|$ in these molecules arises from their unique cylindrical helical conjugated systems. On one hand, this structure arranges the local electric transition dipole moments of the building units in a circular fashion, generating a large induced magnetic transition dipole moment along the helical axis.[48] On the other hand, their high D_n symmetry ensures that μ and m remain parallel or antiparallel, maximizing $|\cos\theta|$ and thus achieving a large $|g_{lum}|$.[44,49] Long et al. further demonstrated through theoretical calculations that increasing the number of building units to synthesize higher-order D_n-symmetric nanorings could
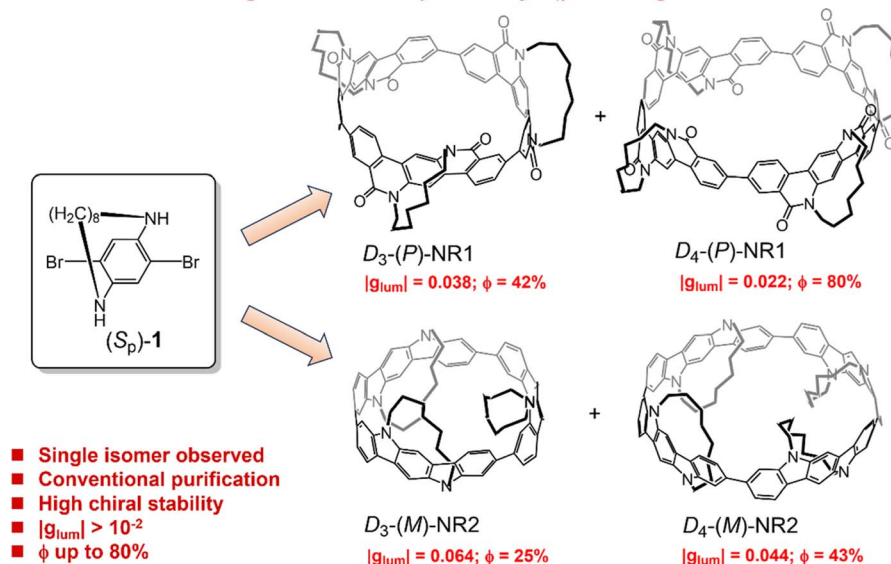

Fig. 1 (a) Previously reported D_n-symmetric chiral conjugated nanorings. (b) Theoretically predicted high-order D_n-nanorings with giant g-values. (c) Chiral tether-guided selective synthesis of D_n-nanorings in this work.

significantly enhance the magnetic transition dipole moment along the helical axis, enabling giant g values (Fig. 1b).[50] For instance, starting from Isobe's [4]CC framework, expanding to a D_8-symmetric [8]CC (8 units) increases g to 0.71, while a D_{20}-symmetric [20]CC (20 units) could further elevate g to 1.47, all while maintaining high transition oscillator strengths.

The above experimental and theoretical studies demonstrate that D_n-symmetric chiral conjugated nanorings represent a highly promising class of molecules, offering potential breakthroughs in organic luminescent materials with intrinsically giant g_{lum} values. However, their synthesis faces a critical challenge: the formation of atropisomers (conformational isomers arising from flipping of building units) during preparation. The number of atropisomers increases rapidly with higher symmetry order (n). Tanaka et al. reported a D_2-symmetric nanoring (S_p,S_p)-(M,M,M,M)-1a, which theoretically has 3 atropisomers (Fig. 1a). While an asymmetric catalytic cyclization enabled the selective synthesis of the D_2-symmetric isomer, its $|g_{lum}|$ was only 0.005.[51] Isobe et al. observed all 4 possible atropisomers in the preparation of D_3-symmetric nanoring (P)-(9,6)-[3]C^{db}C. The optically pure (P)-(9,6)-[3]C^{db}C was obtained via chiral HPLC purification.[48] For D_4-symmetric nanorings, the number of atropisomers rises to 6. Aforementioned (P)-(12,8)-[4]CC and $(+)$-[4]CAn$_{2,6}$ both required laborious chiral HPLC purification.[45,46] For higher-order systems like D_8-symmetric [8]CC and D_{20}-symmetric [20]CC proposed by Long et al., the atropisomer count escalates to 30 and 27012, respectively, making their synthesis and isolation extremely challenging.[50] Thus, developing a method to selectively access D_n-symmetric nanorings is crucial to advance their applications in chiral organic luminescent materials. In this work, we report a novel chiral tether-guided synthesis strategy for D_n-symmetric chiral conjugated nanorings (Fig. 1c). By incorporating a strained planar-chiral alkyl tether into the fused-ring building block of the nanoring, we significantly amplify the energy differences between various atropisomers. This thermodynamic control drives the formation of the most stable D_n-symmetric isomer with exceptional selectivity during synthesis. Using this innovative approach, we successfully synthesized four chiral nanorings: D_3-(P)-NR1, D_4-(P)-NR1, D_3-(M)-NR2, and D_4-(M)-NR2, along with their respective enantiomers. The helical chirality of these molecules is uniquely determined by the planar chirality of their tether moieties. These compounds exhibit remarkable CPL properties, with all derivatives demonstrating $|g_{lum}|$ exceeding 10^{-2}.
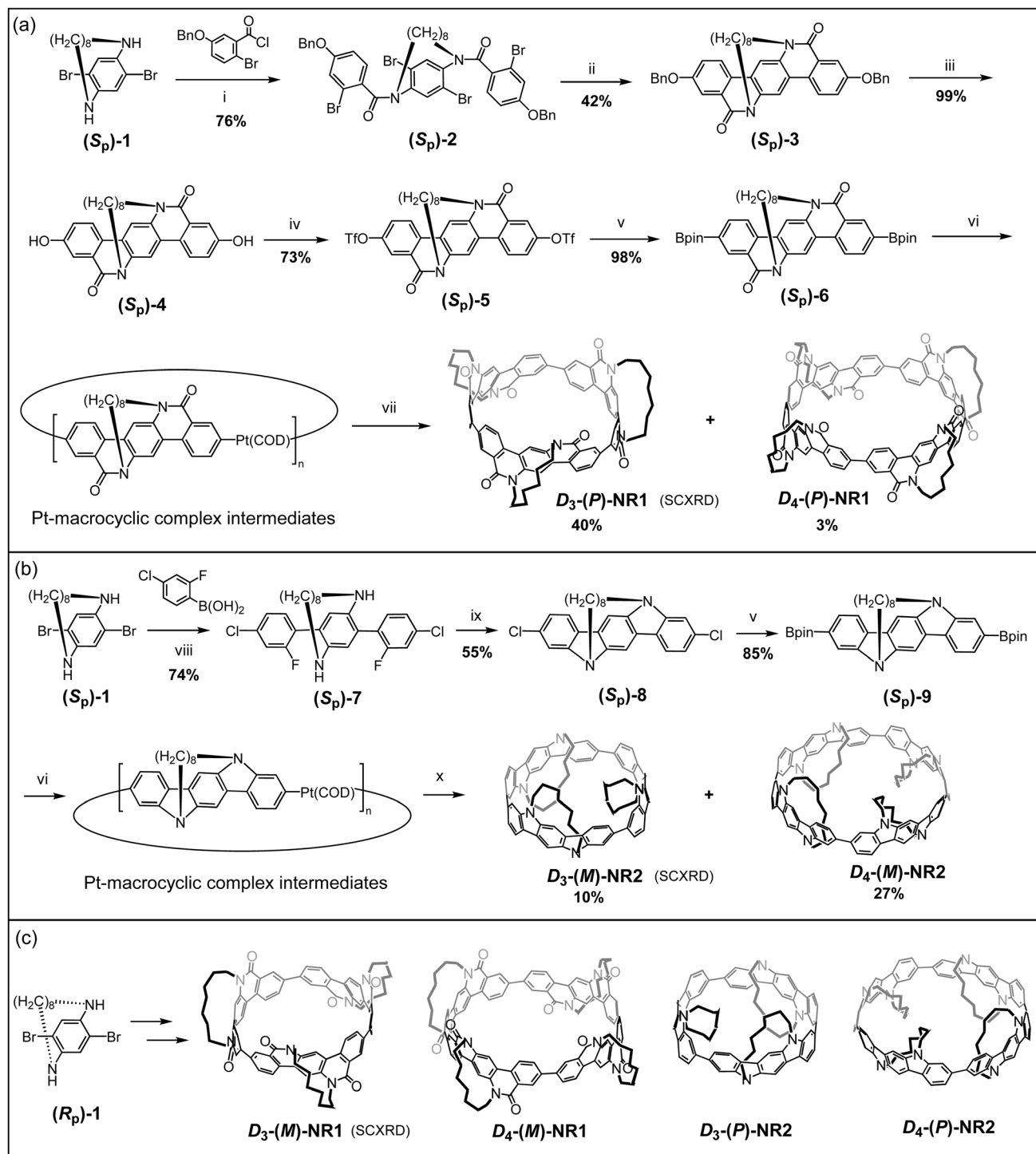
Results and discussion

The synthetic routes for the nanorings are illustrated in Scheme 1. For D_3-(P)-NR1 and D_4-(P)-NR1 (Scheme 1a), starting from the previously reported planar chiral cyclophane (S_p)-1,[52] the synthesis proceeded via acylation to afford the dibenzyloxy-terminated amide (S_p)-2. Subsequent intramolecular Yamamoto cyclization yielded the pentacyclic fused lactam (S_p)-3.[53–55] Deprotection of the benzyl groups followed by acylation furnished the triflate-terminated intermediate (S_p)-5, which was further converted into the boronic ester (S_p)-6 via Pd-catalyzed

borylation. Equimolar reaction of (S_p)-6 with Pt(COD)Cl$_2$ generated the Pt-macrocyclic complex intermediates, and final reductive elimination promoted by PPh$_3$ afforded the chiral trimeric ring D_3-(P)-NR1 and the chiral tetrameric ring D_4-(P)-NR1 in yields of 40% and 3% (starting from (S_p)-6), respectively. The preferential formation of the trimer suggests that the highly curved backbone of the fused-ring unit (S_p)-6 favors smaller macrocycles in this Pt-mediated nanoring synthesis.[48] For D_3-(M)-NR2 and D_4-(M)-NR2 (Scheme 1b), (S_p)-1 first underwent Suzuki coupling with 3-chloro-2-fluorobenzeneboronic acid to afford (S_p)-7, which was cyclized via a potassium tert-butoxide-mediated intramolecular nucleophilic substitution to form the pentacyclic carbazole (S_p)-8.[52,56] Pd-catalyzed borylation then replaced the terminal chlorine with a boronic ester, yielding (S_p)-9. Subsequent Pt-mediated macrocyclization produced the chiral trimer D_3-(M)-NR2 and the chiral tetramer D_4-(M)-NR2 in 10% and 27% yields (starting from (S_p)-9), respectively. Unlike the fused-lactam-based system, the fused-carbazole-derived nanoring predominantly formed the tetrameric product. Using the enantiomeric planar chiral cyclophane (R_p)-1 as the starting material, we also synthesized the enantiomers of the above four nanorings—D_3-(M)-NR1, D_4-(M)-NR1, D_3-(P)-NR2 and D_4-(P)-NR2 (Scheme 1c). Detailed synthetic procedures are provided in the SI (Schemes S3 and S4). It is worth mentioning that all the nanorings were obtained through conventional column chromatography separation, without the need for chiral HPLC purification. All nanoring structures were characterized by NMR and mass spectroscopic methods. Both ^{1}H and ^{13}C NMR spectra confirmed that each nanoring was obtained as a single isomer (see SI). Additionally, single-crystal X-ray diffraction (SCXRD) analysis unambiguously determined the structures of D_3-(P)-NR1, D_3-(M)-NR2, and the enantiomer D_3-(M)-NR1 (vide infra).

The single-crystal structures of D_3-(P)-NR1 and D_3-(M)-NR2 are shown in Fig. 2a, and that for D_3-(M)-NR1 is presented in Fig. S64. Crystallographic data reveal that all molecules adopt a single configuration without other atropisomers, and their ring skeletons exhibit D_3 symmetry. Although both D_3-(P)-NR1 and D_3-(M)-NR2 were synthesized from the same starting material, (S_p)-1, their macrocyclic structures differ significantly. In D_3-(P)-NR1, all the tethers are positioned on the outer periphery of the nanoring, and the three fused-ring lactam building blocks (S_p)-M1 adopt a clockwise P-helical arrangement. In contrast, in D_3-(M)-NR2, all the tethers are oriented inside the nanoring, and the three fused-ring carbazole units (S_p)-M2 form a counterclockwise M-helical arrangement. D_3-(M)-NR1, synthesized from (R_p)-1, shows the mirror-image structure of D_3-(P)-NR1, exhibiting M-helicity (Fig. S64). From the top view (Fig. 2b), the diameter of the lactam nanoring D_3-(P)-NR1 is larger ($\sim$12.7 Å), whereas that of the carbazole nanoring D_3-(M)-NR2 is slightly smaller ($\sim$12.1 Å). Regarding packing structures, D_3-(P)-NR1 molecules form a 2D layered arrangement, where adjacent nanorings within each layer are nearly perpendicular, resembling a herringbone pattern—similar to some known cycloparaphenylene (CPP) nanorings (e.g., [6]CPP, [7]CPP).[57,58] In contrast, D_3-(M)-NR2 crystals exhibit a triangular packing motif: three nanoring molecules assemble into a circular

Scheme 1 Synthetic routes for (a) D_3-(P)-NR1 and D_4-(P)-NR1, (b) D_3-(M)-NR2 and D_4-(M)-NR2, and (c) the enantiomers. Reaction conditions: (i) Et$_3$N, 70 °C; (ii) Ni(COD)$_2$/2,2'-bipyridine, 70 °C; (iii) Pd/C, NH$_4$OOCH, 80 °C; (iv) Tf$_2$O/pyridine; (v) (Bpin)$_2$, Pd(OAc)$_2$/S-Phos, 80 °C; (vi) (COD)PtCl$_2$, CsF; (vii) PPh$_3$, 110 °C; (viii) Pd(PPh$_3$)$_4$, K$_2$CO$_3$, 70 °C; (ix) ^{t}BuOK, 80 °C; (x) PPh$_3$, 150 °C.

trimer, with disordered solvent molecules filling the triangular pores. This arrangement resembles the triangular stacking observed in Itami's previously reported carbon nanobelts (CNB) (e.g., [24]CNB).[55] To understand why D_3-(P)-NR1 has all tethers outward while D_3-(M)-NR2 has them inward, we examined the conformations of their building blocks, (S_p)-M1 and (S_p)-M2

(Fig. 2c). DFT-optimized structures show that the fused-ring backbone of (S_p)-M1 bends outward due to tether-induced strain, favoring an exterior tether placement, whereas (S_p)-M2 bends inward under the strain, directing its tethers inside the nanoring.
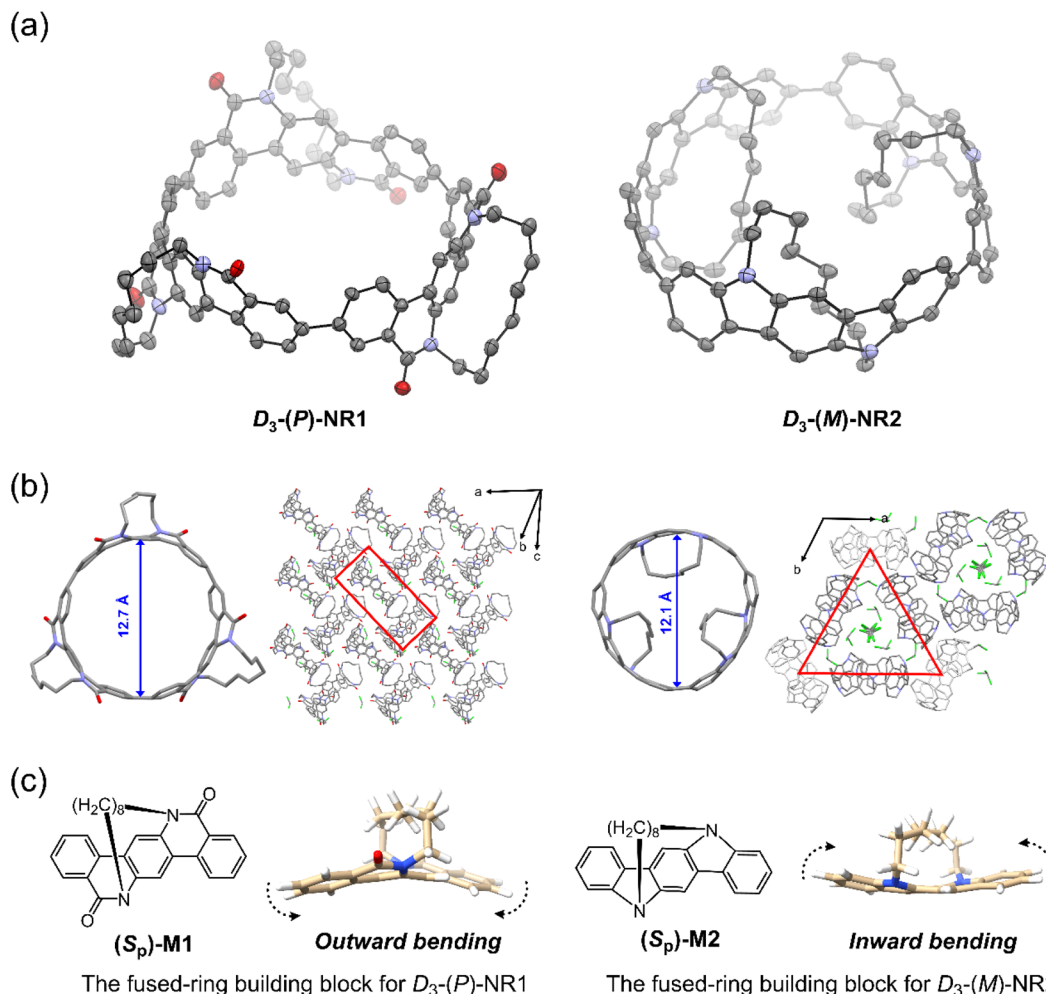
Fig. 2 (a) Single crystal structures for D_3-(P)-NR1 and D_3-(M)-NR2; (b) top view and packing structures for D_3-(P)-NR1 and D_3-(M)-NR2; (c) the fused-ring building blocks (S_p)-M1 and (S_p)-M2, and their DFT-optimized configurations. Note: the solvent systems used for single-crystal growth are hexane/dichloromethane and methanol/chloroform for D_3-(P)-NR1 and D_3-(M)-NR2, respectively; the solvent molecules in the crystals of D_3-(P)-NR1 and D_3-(M)-NR2 are dichloromethane and chloroform, respectively.

To elucidate the high selectivity in obtaining D_n-symmetric nanorings without observable formation of other atropisomeric products, we calculated the energies of all possible atropisomers. For comparison, we also calculated the energies of hypothetical tether-free nanorings (where one alkyl tether is replaced by two methyl groups). Fig. 3 shows the relative Gibbs free energies of all four possible atropisomers for the D_3-symmetric nanorings (D_3-(P)-NR1 and D_3-(M)-NR2) and their tether-free analogues. For D_3-(P)-NR1 and D_3-(M)-NR2, the lowest-energy isomers are Aooo and Biii ('o' (outside) and 'i' (inside) describe the tether's position with respect to the nanoring), respectively. These structures match the single-crystal configurations. Flipping one fused-ring unit to form Aooi and Biio raises the energy by 8.4 kcal mol^{-1} and 24.6 kcal mol^{-1}, respectively. Obviously, the D_3-symmetric Aooo and Biii are much favored energetically over other isomers. On the other hand, the tether-free analogues exhibit low energy differences (a few kcal mol^{-1}) among atropisomers ('a' and 'b' denote the syn-facial and $anti$-facial arrangement of the fused-

ring building units) (Fig. 3c and d), consistent with prior reports.[59] Similar energies imply the lack of a dominant product, as all are likely to form during the synthesis. The above results indicate that by introducing strained chiral tethers into the nanoring significantly increases the energy differences among atropisomers, thereby enabling one D_n-symmetric isomer to become the dominant product and greatly enhancing selectivity. We also conducted energy analyses on all atropisomers of the D_4-symmetric nanorings D_4-(P)-NR1, D_4-(M)-NR2, and their tether-free analogues, arriving at the same conclusion (Fig. S65 and S66). Notably, the tether does not significantly affect the rotational barriers between the atropisomers. Similar to the tether-free nanorings, D_3-(P)-NR1, D_3-(M)-NR2, D_4-(P)-NR1, and D_4-(M)-NR2 all exhibit high atropisomerization barriers (21.4–67.5 kcal mol^{-1}), indicating that they can maintain stable helical configurations with high chiral stability (Fig. S65 and S66).

The striking structural difference between the fused-lactam nanorings (D_3-(P)-NR1 and D_4-(P)-NR1) and fused-carbazole
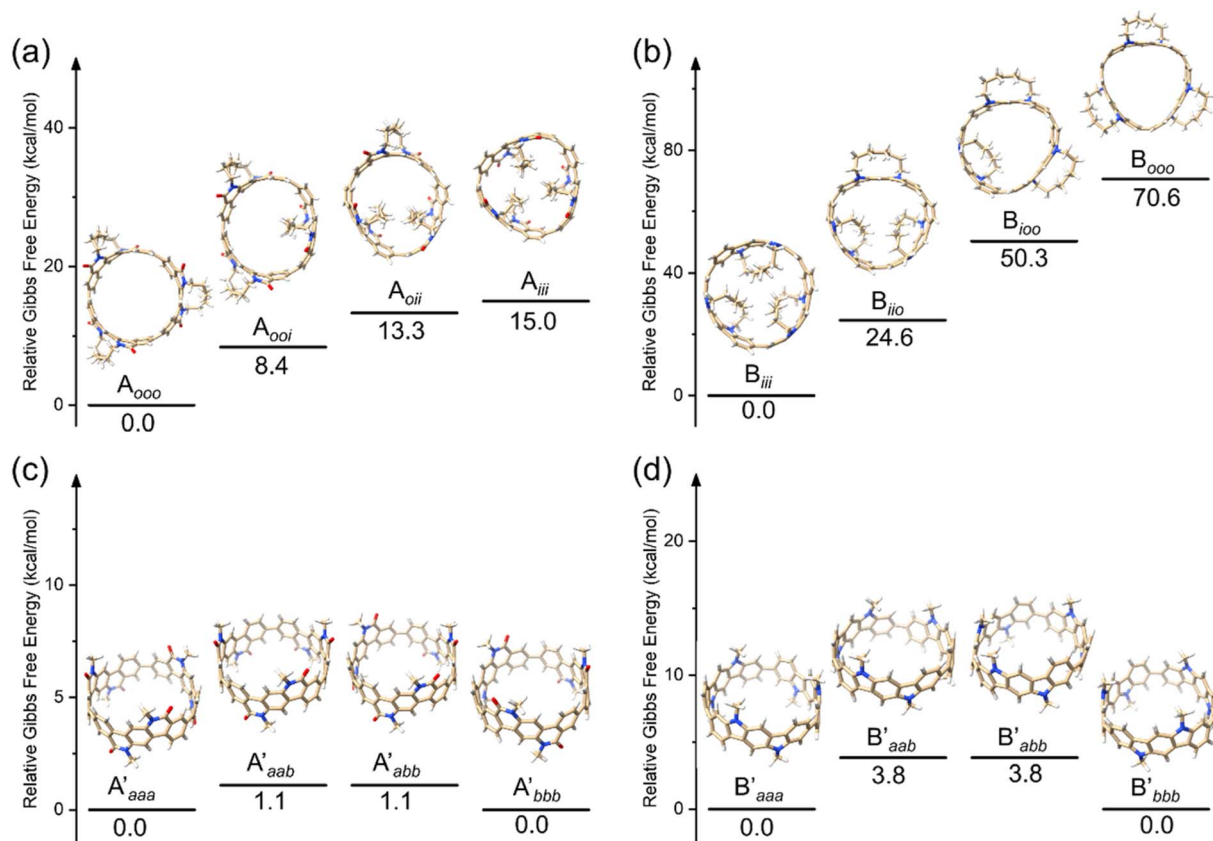
Fig. 3 The relative Gibbs free energies for different atropisomers of (a) D_3-(P)-NR1 (A series), (b) D_3-(M)-NR2 (B series) and the tether-free analogues of (c) D_3-(P)-NR1 (A′ series) and (d) D_3-(M)-NR2 (B′ series).

nanorings (D_3-(M)-NR2 and D_4-(M)-NR2), where the tethers are positioned exteriorly and interiorly respectively, results in significantly distinct chemical shifts of the tether protons in NMR spectra. Particularly, the most pronounced shift is observed for proton H_1, which is closest to the central benzene ring of the building block (Fig. 4a). For the fused-lactam building unit (S_p)-M1, its H_1 appears at −0.29 ppm due to its location above the central benzene ring, where it experiences shielding effects and resonates in a relatively upfield region. However, upon incorporation into nanorings D_3-(P)-NR1 and D_4-(P)-NR1, the chemical shift of H_1 moves to 0.68 ppm and 0.57 ppm respectively, indicating markedly reduced shielding in the exterior regions of the nanorings. Conversely, for the fused-carbazole building unit (S_p)-M2, H_1 initially appears at −1.86 ppm. After being integrated into nanorings D_3-(M)-NR2 and D_4-(M)-NR2, its chemical shift moves to −3.90 ppm and −3.11 ppm, respectively, demonstrating enhanced shielding within the interior cavity of the nanorings. These experimental observations align well with the trends predicted by DFT calculations. Previous theoretical studies have proposed that the exterior and interior of certain cyclic nanocarbons correspond to less-shielded and shielded regions, respectively.[60] In this study, H_1 worked as an NMR probe, providing direct experimental evidence. To further investigate the magnetic shielding environments, we computed the nucleus-independent chemical shift (NICS)[61–63] of the central benzene

rings (Fig. 4b). The results reveal that for all nanorings, the NICS(−1) values (interior) are consistently more negative than the NICS(1) values (exterior), confirming stronger shielding inside the rings, in agreement with our NMR observations. Moreover, compared to the building blocks, all nanorings exhibit less negative NICS(1) values, while the NICS(−1) values tend to become more negative (except for D_4-(M)-NR2, which shows minimal change). This suggests that upon nanoring formation, the increased curvature of the building units leads to reduced shielding on the convex side (exterior) and enhanced shielding on the concave side (interior), consistent with prior literature reports.[64,65] The average values (NICS$_{avg}$) of NICS(1) and NICS(−1) show a clear trend toward less negative values from monomers to nanorings, indicating reduced aromaticity of the central benzene ring due to heightened curvature in the nanoring structures.

Next, we investigated the optical properties of the nanorings. Fig. 5a displays the UV-Vis absorption spectra of D_3-(P)-NR1, D_4-(P)-NR1, D_3-(M)-NR2 and D_4-(M)-NR2. Their respective enantiomers, D_3-(M)-NR1, D_4-(M)-NR1, D_3-(P)-NR2 and D_4-(P)-NR2, show identical spectra (Fig. S67). It can be observed that the spectra of the fused-lactam nanorings D_3-(P)-NR1 and D_4-(P)-NR1 primarily exhibit two absorption bands (one at 320–400 nm and another at 400–500 nm), whereas the fused-carbazole nanorings D_3-(M)-NR2 and D_4-(M)-NR2 show only one main absorption band at 320–420 nm. This difference is mainly attributed to the
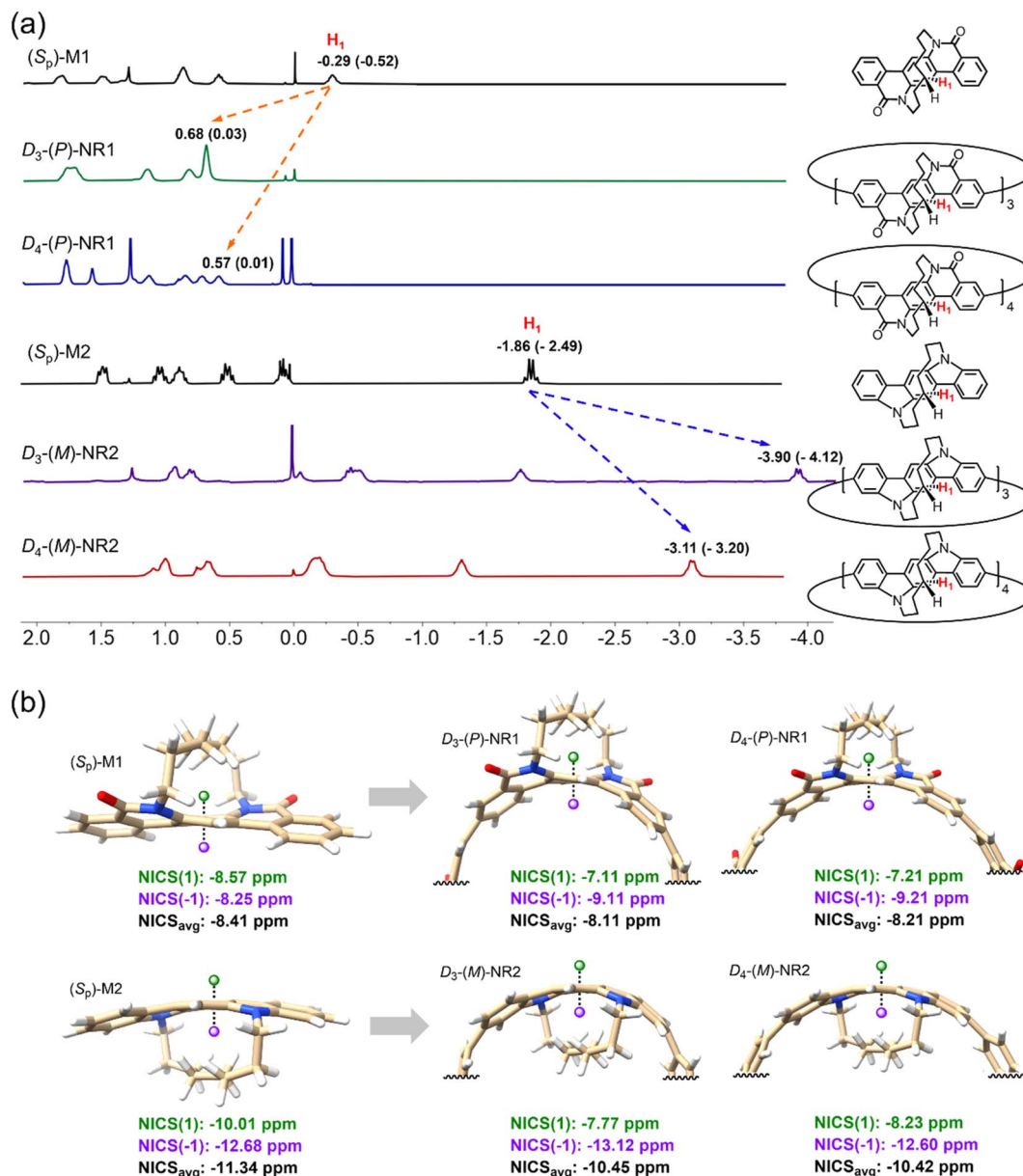
Fig. 4 (a) The change of the NMR chemical shifts (the values in parentheses are DFT-calculated chemical shifts) of proton H_1 from building blocks to nanorings; (b) the calculated NICS(1), NICS(−1) and the averages of NICS(1) and NICS(−1) for the building blocks and nanorings.

fact that some lower-energy electronic transitions (*e.g.*, $S_0 \rightarrow S_2$, $S_0 \rightarrow S_3$) in the fused-lactam nanorings exhibit higher oscillator strengths (Table S1). The oscillator strengths of the $S_0 \rightarrow S_1$ transitions are very low for all nanorings, likely due to the high molecular symmetry, which makes the $S_0 \rightarrow S_1$ transition forbidden. Consequently, the absorption coefficients near the bandgap are relatively low for all nanorings. From the onset absorption, the optical bandgaps of D_3-(*P*)-NR1, D_4-(*P*)-NR1, D_3-(*M*)-NR2 and D_4-(*M*)-NR2 are calculated to be 2.40, 2.51, 2.54, and 2.62 eV, respectively. It is evident that, for both fused-lactam and fused-carbazole nanorings, the smaller-sized nanorings possess narrower bandgaps than their larger-sized counterparts, consistent with previously reported trends for CPP and CNB nanorings.[22,55,66] DFT calculations further confirm

this observation, showing that smaller-sized nanorings have smaller HOMO–LUMO gaps (Fig. S69). Additionally, theoretical calculations indicate that the fused-carbazole nanorings have higher HOMO and LUMO energy levels compared to the fused-lactam nanorings, which aligns with the energy levels measured in electrochemical experiments (Fig. S70). The photo-luminescence spectra of all nanorings and their enantiomers are shown in Fig. 5b and S71, respectively. All samples were measured in toluene solution. The excitation wavelengths were set at 360 nm for D_3-(*P/M*)-NR1, 370 nm for D_4-(*P/M*)-NR1, and 380 nm for both D_3-(*M/P*)-NR2 and D_4-(*M/P*)-NR2. The fluorescence peaks of D_3-(*P*)-NR1, D_4-(*P*)-NR1, D_3-(*M*)-NR2 and D_4-(*M*)-NR2 are located at 561, 520, 519, and 492 nm, respectively. The measured fluorescence quantum yields are 42%, 80%, 25%, and
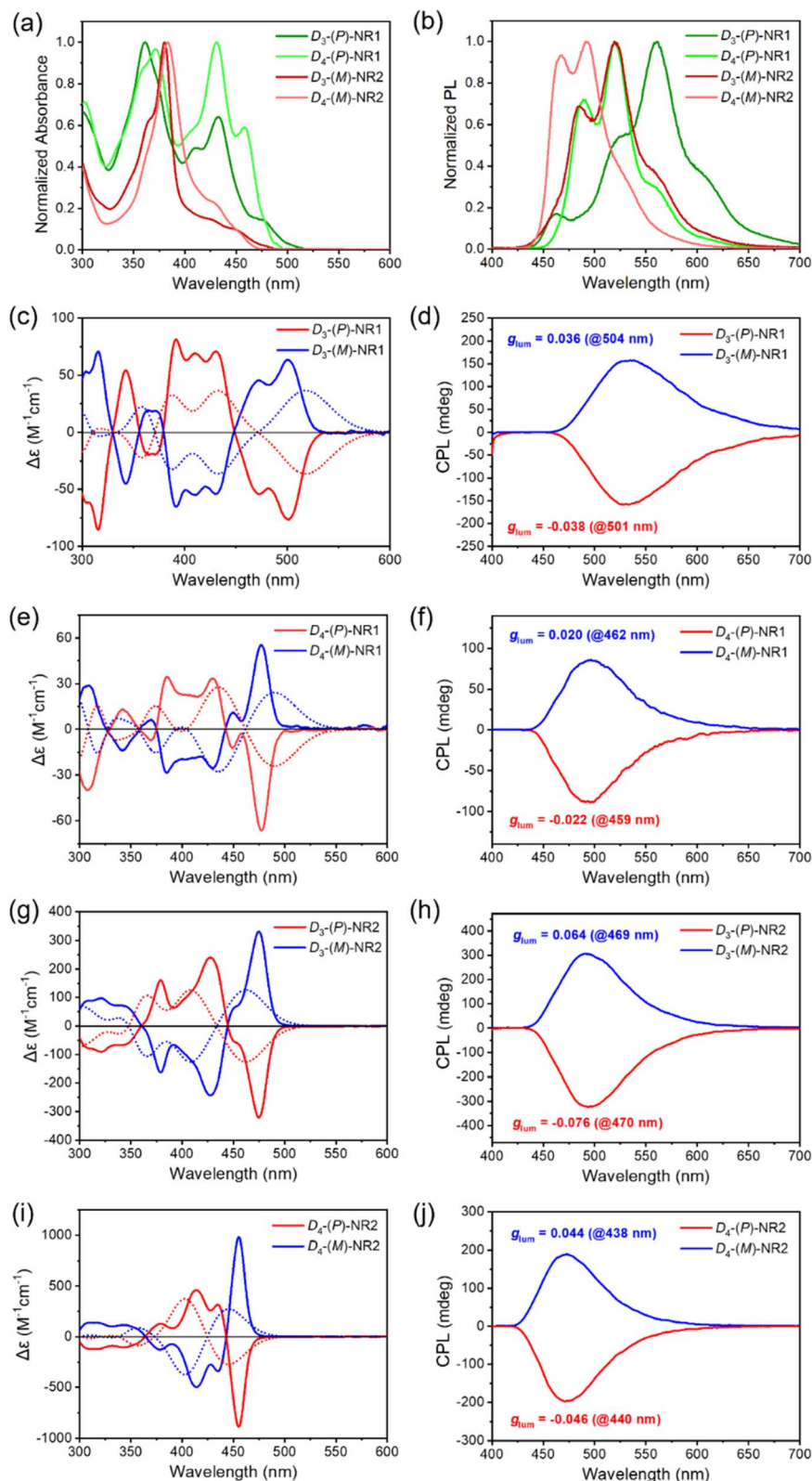
Fig. 5 The UV-Vis absorption spectra (a) and photoluminescence spectra (b) for D_3-(P)-NR1, D_4-(P)-NR1, D_3-(M)-NR2 and D_4-(M)-NR2. The CD (left) and CPL (right) spectra for D_3-(P)-NR1 and D_3-(M)-NR1 (c and d), D_4-(P)-NR1 and D_4-(M)-NR1 (e and f), D_3-(P)-NR2 and D_3-(M)-NR2 (g and h), D_4-(P)-NR2 and D_4-(M)-NR2 (i and j) in toluene. Note: the dotted lines in the CD spectra are DFT-predicted ones.

43%, respectively. Notably, compared to the larger D_4 nanorings, the smaller D_3 nanorings exhibit red-shifted emission peaks and reduced quantum yields, similar to the size-dependent luminescence properties observed in CPP and methylene-bridged cycloparaphenylene (MCPP) nanorings.[67–69]

Since the nanorings prepared *via* the chiral tether-guided approach possess uniquely defined configurations, chiral resolution is unnecessary, allowing direct testing of their chiroptical properties. The circular dichroism (CD) and circularly polarized luminescence (CPL) spectra of all nanorings and their enantiomers are shown in Fig. 5c–j. All measurements were conducted in dilute solutions ($\sim 1 \times 10^{-5}$ M) to ensure the signals originated from single molecules rather than aggregates. Each pair of enantiomers exhibited mirror-image CD and CPL spectra. For the CD spectra, all *P*-helical nanorings displayed a negative Cotton effect near the bandgap, while all *M*-helical nanorings showed a positive Cotton effect. The theoretically calculated CD spectra matched well with the experimental results. We further compared the CD spectra of the fused-lactam nanorings D_3-(*P*)-NR1 and D_4-(*P*)-NR1 before and after heating at 100 °C for 24 hours (Fig. S72a), revealing nearly overlapping spectra. Since the fused-carbazole nanorings D_3-(*M*)-NR2 and D_4-(*M*)-NR2 decompose upon heating, we assessed their chiral stability at room temperature. After one week of storage, no significant changes were observed in their CD spectra (Fig. S72b). These experiments confirm the earlier theoretical predictions that these molecules generally possess high atropisomerization barriers (Fig. S65), ensuring excellent chiral stability. All nanorings exhibited strong CPL signals. Consistent with the CD signals near the bandgap, all *P*-helical nanorings displayed a negative Cotton effect in CPL, while all *M*-helical nanorings showed a positive Cotton effect. Additionally, all nanorings demonstrated large luminescence dissymmetry factors (g_{lum}), exceeding 10^{-2} in magnitude. Notably, D_3-(*P*)-NR2 exhibited a remarkably high g_{lum} of -0.076, making it one of the rare purely organic molecules with a large intrinsic g_{lum}. To understand why these nanorings generally exhibit large dissymmetry factors, we analyzed their $S_1 \rightarrow S_0$ transitions by DFT. Fig. 6 illustrates their transition characteristics, revealing that all molecules possess a substantial magnetic transition dipole moment (m) along the helical axis. The $|m|$ values for D_3-(*P*)-NR1, D_4-(*P*)-NR1, D_3-(*M*)-NR2 and D_4-(*M*)-NR2 are 8.32, 12.55, 9.14, and 14.18 Bohr magnetons (μ_B), respectively—among the largest reported for organic chiral molecules.[70] Moreover, the electric (μ) and magnetic (m) transition dipole moments are consistently aligned either parallel or antiparallel. In *P*-helical nanorings, the angles between μ and m are 179.5° and 180°, whereas in *M*-helical nanorings, they are 1.3° and 0°. These factors collectively contribute to the high g_{lum}. Furthermore, the carbazole-type nanorings exhibited larger m and smaller μ compared to the lactam-type nanorings, explaining their higher g_{lum} values. In both carbazole- and lactam-type nanorings, m increased with ring size, consistent with the reported "molecular solenoid inner area rule".[70] From D_3 to D_4 nanorings, the increase in m was comparable to that in μ, resulting in minor changes (or even slight decreases) in g_{lum}. However, based on theoretical calculations by Long *et al.*, synthesizing higher-order
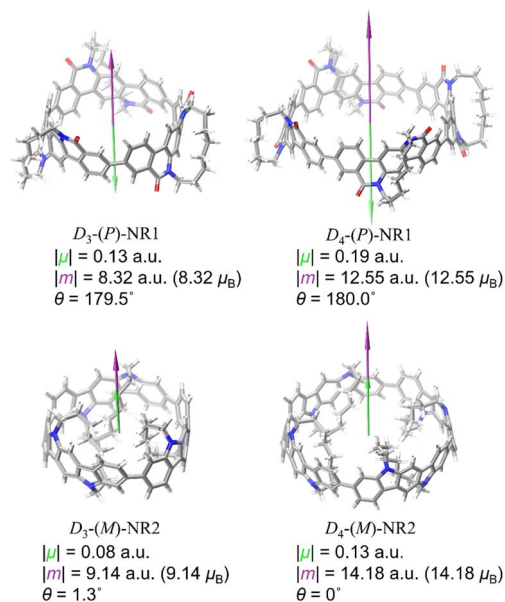

Fig. 6 The optimized geometry of S_1 state and the $S_1 \rightarrow S_0$ transition characteristics for D_3-(*P*)-NR1, D_4-(*P*)-NR1, D_3-(*M*)-NR2 and D_4-(*M*)-NR2. Note: "a.u." denotes the atomic unit; the vector arrow for μ is scaled up by a factor of 60.

D_n-symmetric nanorings could further enhance m relative to μ, potentially leading to breakthroughs in g-values.[50]

Conclusion

In summary, we have developed a chiral tether-guided strategy to selectively prepare D_n-symmetric chiral conjugated nanorings. The high selectivity stems from the chiral tether induced strain, which amplifies the energy differences among the various atropisomers of the nanorings, thereby directing one D_n-symmetric isomer to become the thermodynamically favored product. All synthesized D_3 and D_4 nanorings exhibit exceptional circularly polarized luminescence properties, with a maximum luminescence dissymmetry factor reaching 0.076 and photoluminescence quantum yields up to 80%, demonstrating their great potential as high-performance CPL emitters. In the future, we will extend this strategy to synthesize higher-order D_n-symmetric nanorings, which may lead to breakthroughs in the development of organic molecules with intrinsically giant g_{lum}.

Author contributions

Z. X. conceptualized the work. T. A., Q. Y., Y. S., Z. D., X. Z. synthesized the compounds. T. A. and Y. W. performed the theoretical calculations. J. Y., Z. X., Y. G., Z. H., C. Z. and L. D. directed the experiments and discussed the results. Z. X., Z. H., M. L., C. Z. and L. D. directed the project. Z. X. wrote the manuscript.

Conflicts of interest

The authors declare no conflict of interest.

Data availability

CCDC 2440960, 2440962 and 2440966 contain the supplementary crystallographic data for this paper.[71a-c]

All other data supporting the findings of this study are available within the article and its supplementary information (SI), as well as available from the corresponding authors upon reasonable request. Supporting information available: materials synthesis and characterization; theoretical calculation; Scheme S1–5, Fig. S1–72, Table S1. See DOI: https://doi.org/10.1039/d5sc06445g.

Acknowledgements

References

1 T. Zhang, Y. Xiao, H. Wang, S. Kong, R. Huang, V. Ka-Man Au, T. Yu and W. Huang, Highly Twisted Thermally Activated Delayed Fluorescence (Tadf) Molecules and Their Applications in Organic Light-Emitting Diodes (Oleds), *Angew. Chem., Int. Ed.*, 2023, **62**, e202301896.

2 A. Concellón, J. Castro-Esteban and T. M. Swager, Ultratrace Pfas Detection Using Amplifying Fluorescent Polymers, *J. Am. Chem. Soc.*, 2023, **145**, 11420–11430.

3 Y. Huang, W. Chen, J. Chung, J. Yin and J. Yoon, Recent Progress in Fluorescent Probes for Bacteria, *Chem. Soc. Rev.*, 2021, **50**, 7725–7744.

4 W. Xu, Q. He and J. Cheng, Organic Semiconductor Fluorescent Sensing Materials and Hazardous Chemicals Detection Applications, *Sci. Sin Chem.*, 2020, **50**, 92–107.

5 G. Yin, J. Zhou, W. Lu, L. Li, D. Liu, M. Qi, B. Z. Tang, P. Théato and T. Chen, Targeting Compact and Ordered Emitters by Supramolecular Dynamic Interactions for High-Performance Organic Ambient Phosphorescence, *Adv. Mater.*, 2024, **36**, 2311347.

6 H. Zhu, J. Fan, J. Du and X. Peng, Fluorescent Probes for Sensing and Imaging within Specific Cellular Organelles, *Acc. Chem. Res.*, 2016, **49**, 2115–2126.

7 Y. Zhang, J. Guan, L. Luo, X. Han, J. Wang, Y. Zheng and J. Xu, Chiral Twisted Molecular Carbons: Synthesis, Properties, and Applications, *Interdiscip. Mater.*, 2024, **3**, 453–479.

8 M. Zhang, Q. Guo, Z. Li, Y. Zhou, S. Zhao, Z. Tong, Y. Wang, G. Li, S. Jin, M. Zhu, *et al.*, Processable Circularly Polarized Luminescence Material Enables Flexible Stereoscopic 3D Imaging, *Sci. Adv.*, 2023, **9**, eadi9944.

9 B. L. Feringa, R. A. van Delden, N. Koumura and E. M. Geertsema, Chiroptical Molecular Switches, *Chem. Rev.*, 2000, **100**, 1789–1816.

10 P. Stachelek, S. Serrano-Buitrago, B. L. Maroto, R. Pal and S. de la Moya, Circularly Polarized Luminescence Bioimaging Using Chiral Bodipys: A Model Scaffold for Advancing Unprecedented CPL Microscopy Using Small Full-Organic Probes, *ACS Appl. Mater. Interfaces*, 2024, **16**, 67246–67254.

11 I. Song, J. Ahn, H. Ahn, S. H. Lee, J. Mei, N. A. Kotov and J. H. Oh, Helical Polymers for Dissymmetric Circularly Polarized Light Imaging, *Nature*, 2023, **617**, 92–99.

12 X. Liang, W. Liang, P. Jin, H. Wang, W. Wu and C. Yang, Advances in Chirality Sensing with Macrocyclic Molecules, *Chemosensors*, 2021, **9**, 279.

13 T. Kawasaki, M. Sato, S. Ishiguro, T. Saito, Y. Morishita, I. Sato, H. Nishino, Y. Inoue and K. Soai, Enantioselective Synthesis of near Enantiopure Compound by Asymmetric Autocatalysis Triggered by Asymmetric Photolysis with Circularly Polarized Light, *J. Am. Chem. Soc.*, 2005, **127**, 3274–3275.

14 Z. Shang, T. Liu, Q. Yang, S. Cui, K. Xu, Y. Zhang, J. Deng, T. Zhai and X. Wang, Chiral-Molecule-Based Spintronic Devices, *Small*, 2022, **18**, 2203015.

15 W. Chen, B. Li, G. Gao and T. Sun, Chiral Supramolecular Nanomaterials: From Chirality Transfer and Amplification to Regulation and Applications, *Interdiscip. Mater.*, 2023, **2**, 689–713.

16 L. Liu, Y. Yang and Z. Wei, Chiral Organic Optoelectronic Materials and Circularly Polarized Light Luminescence and Detection, *Acta Chim. Sinica*, 2022, **80**, 970–992.

17 F. S. Richardson and J. P. Riehl, Circularly Polarized Luminescence Spectroscopy, *Chem. Rev.*, 1977, **77**, 773–792.

18 E. M. Sánchez-Carnerero, A. R. Agarrabeitia, F. Moreno, B. L. Maroto, G. Muller, M. J. Ortiz and S. de la Moya, Circularly Polarized Luminescence from Simple Organic Molecules, *Chem.–Eur. J.*, 2015, **21**, 13488–13500.

19 M. Kasha, Characterization of Electronic Transitions in Complex Molecules, *Discuss. Faraday Soc.*, 1950, **9**, 14–19.

20 T. Zhao, J. Han, P. Duan and M. Liu, New Perspectives to Trigger and Modulate Circularly Polarized Luminescence of Complex and Aggregated Systems: Energy Transfer, Photon Upconversion, Charge Transfer, and Organic Radical, *Acc. Chem. Res.*, 2020, **53**, 1279–1292.

21 Z.-L. Gong, X. Zhu, Z. Zhou, S.-W. Zhang, D. Yang, B. Zhao, Y.-P. Zhang, J. Deng, Y. Cheng, Y.-X. Zheng, *et al.*, Frontiers in Circularly Polarized Luminescence: Molecular Design, Self-Assembly, Nanomaterials, and Applications, *Sci. China Chem.*, 2021, **64**, 2060–2104.

22 S. Guo, L. Liu, X. Li, G. Liu, Y. Fan, J. He, Z. Lian, H. Yang, X. Chen and H. Jiang, Highly Luminescent Chiral Carbon Nanohoops *Via* Symmetry Breaking with a Triptycene Unit: Bright Circularly Polarized Luminescence and Size-Dependent Properties, *Small*, 2024, **20**, 2308429.

23 Y. Liu, Z. Li, M.-W. Wang, J. Chan, G. Liu, Z. Wang and W. Jiang, Highly Luminescent Chiral Double π-Helical Nanoribbons, *J. Am. Chem. Soc.*, 2024, **146**, 5295–5304.

24 Z. Sun, W. Xu, S. Qiu, Z. Ma, C. Li, S. Zhang and H. Wang, Thia[n]helicenes with Long Persistent Phosphorescence, *Chem. Sci.*, 2024, **15**, 1077–1087.

25 L. Bian, M. Tang, J. Liu, Y. Liang, L. Wu and Z. Liu, Luminescent Chiral Triangular Prisms Capable of Forming Double Helices for Detecting Traces of Acids and Anion Recognition, *J. Mater. Chem. C*, 2022, **10**, 15394–15399.

26 X. Kong, X. Zhang, B. Yuan, W. Zhang, D. Lu and P. Du, Synthesis and Photophysical Properties of a Chiral Carbon Nanoring Containing Rubicene, *J. Org. Chem.*, 2024, **89**, 8255–8261.

27 G. Li, L.-L. Mao, J.-N. Gao, X. Shi, Z.-Y. Huo, J. Yang, W. Zhou, H. Li, H.-B. Yang, C.-H. Tung, *et al.*, A Helical Tubular Dyad of [9]Cycloparaphenylene: Synthesis, Chiroptical Properties and Post-Functionalization, *Angew. Chem., Int. Ed.*, 2025, **64**, e202419435.

28 Y.-F. Wu, S.-W. Ying, L.-Y. Su, J.-J. Du, L. Zhang, B.-W. Chen, H.-R. Tian, H. Xu, M.-L. Zhang, X. Yan, *et al.*, Nitrogen-Embedded Quintuple [7]Helicene: A Helicene–Azacorannulene Hybrid with Strong near-Infrared Fluorescence, *J. Am. Chem. Soc.*, 2022, **144**, 10736–10742.

29 F. Zhao, J. Zhao, H. Liu, Y. Wang, J. Duan, C. Li, J. Di, N. Zhang, X. Zheng and P. Chen, Synthesis of π-Conjugated Chiral Organoborane Macrocycles with Blue to near-Infrared Emissions and the Diradical Character of Cations, *J. Am. Chem. Soc.*, 2023, **145**, 10092–10103.

30 X.-Y. Wang, J. Bai, Y.-J. Shen, Z.-A. Li and H.-Y. Gong, A Carbazole-Centered Expanded Helicene Stabilized with Hexabenzocoronene (HBC) Units, *Angew. Chem., Int. Ed.*, 2025, **64**(1), e202417745.

31 Y. Chen, C. Lin, Z. Luo, Z. Yin, H. Shi, Y. Zhu and J. Wang, Double π-Extended Undecabenzo[7]helicene, *Angew. Chem., Int. Ed.*, 2021, **60**, 7796–7801.

32 J.-K. Li, X.-Y. Chen, W.-L. Zhao, Y.-L. Guo, Y. Zhang, X.-C. Wang, A. C.-H. Sue, X.-Y. Cao, M. Li, C.-F. Chen, *et al.*, Synthesis of Highly Luminescent Chiral Nanographene, *Angew. Chem., Int. Ed.*, 2023, **62**, e202215367.

33 Y. Zhu, G. Chen, Y. Deng, H. Yang, C. Wang, J. Gao, C. Zhang and J. Xiao, Synthesis and Characterization of Asymmetric Azatwistarenes with Chiroptical Property, *Org. Lett.*, 2024, **26**, 9486–9491.

34 J. Hu, Q. Xiang, X. Tian, L. Ye, Y. Wang, Y. Ni, X. Chen, Y. Liu, G. Chen and Z. Sun, S-Shaped Helical Singlet Diradicaloid and Its Transformation to Circumchrysene *via* a Two-Stage Cyclization, *J. Am. Chem. Soc.*, 2024, **146**, 10321–10330.

35 G.-F. Huo, W.-T. Xu, J. Hu, Y. Han, W. Fan, W. Wang, Z. Sun, H.-B. Yang and J. Wu, Perylene-Embedded Helical Nanographenes with Emission up to 1010 nm: Synthesis, Structures, and Chiroptical Properties, *Angew. Chem., Int. Ed.*, 2025, **64**, e202416707.

36 D. Yang, K. M. Cheung, Q. Gong, L. Zhang, L. Qiao, X. Chen, Z. Huang and Q. Miao, Synthesis, Structures and Properties of Trioxa[9]circulene and Diepoxycyclononatrinaphthalene, *Angew. Chem., Int. Ed.*, 2024, **63**, e202402756.

37 W. Niu, Y. Fu, Z.-L. Qiu, C. J. Schürmann, S. Obermann, F. Liu, A. A. Popov, H. Komber, J. Ma and X. Feng, π-Extended Helical Multilayer Nanographenes with Layer-Dependent Chiroptical Properties, *J. Am. Chem. Soc.*, 2023, **145**, 26824–26832.

38 G.-F. Huo, T. M. Fukunaga, X. Hou, Y. Han, W. Fan, S. Wu, H. Isobe and J. Wu, Facile Synthesis and Chiral Resolution of Expanded Helicenes with up to 35 cata-Fused Benzene Rings, *Angew. Chem., Int. Ed.*, 2023, **62**, e202218090.

39 M. Krzeszewski, H. Ito and K. Itami, Infinitene: A Helically Twisted Figure-Eight [12]Circulene Topoisomer, *J. Am. Chem. Soc.*, 2022, **144**, 862–871.

40 Y. Matsuo, M. Gon, K. Tanaka, S. Seki and T. Tanaka, Synthesis of Aza[n]helicenes up to n = 19: Hydrogen-Bond-Assisted Solubility and Benzannulation Strategy, *J. Am. Chem. Soc.*, 2024, **146**, 17428–17437.

41 X. Xiao, Q. Cheng, S. T. Bao, Z. Jin, S. Sun, H. Jiang, M. L. Steigerwald and C. Nuckolls, Single-Handed Helicene Nanoribbons *Via* Transfer of Chiral Information, *J. Am. Chem. Soc.*, 2022, **144**, 20214–20220.

42 R. Ammenhäuser, J. M. Lupton and U. Scherf, Chain-Length Dependence of the Optical Activity of Helical Triptycene-Based π-Conjugated Ladder Polymers, *Adv. Opt. Mater.*, 2024, **12**, 2301857.

43 S. Jena, A. Thayyil Muhammed Munthasir, S. Pradhan, M. Kitahara, S. Seika, Y. Imai and P. Thilagar, Single Molecular Persistent Room-Temperature Phosphorescence and Circularly Polarized Luminescence from Binaphthol-Decorated Optically Innocent Cyclotriphosphazenes, *Chem.–Eur. J.*, 2023, **29**, e202301924.

44 H. Kubo, D. Shimizu, T. Hirose and K. Matsuda, Circularly Polarized Luminescence Designed from Molecular Orbitals: A Figure-Eight-Shaped [5]Helicene Dimer with D2 Symmetry, *Org. Lett.*, 2020, **22**, 9276–9281.

45 S. Sato, A. Yoshii, S. Takahashi, S. Furumi, M. Takeuchi and H. Isobe, Chiral Intertwined Spirals and Magnetic Transition Dipole Moments Dictated by Cylinder Helicity, *Proc. Natl. Acad. Sci. U. S. A*, 2017, **114**, 13097–13101.

46 J. Wang, G. Zhuang, M. Chen, D. Lu, Z. Li, Q. Huang, H. Jia, S. Cui, X. Shao, S. Yang, *et al.*, Selective Synthesis of Conjugated Chiral Macrocycles: Sidewall Segments of (−)/(+)-(12,4) Carbon Nanotubes with Strong Circularly Polarized Luminescence, *Angew. Chem., Int. Ed.*, 2020, **59**, 1619–1626.

47 F. Xu, H. Su, J. J. B. van der Tol, S. A. H. Jansen, Y. Fu, G. Lavarda, G. Vantomme, S. Meskers and E. W. Meijer, Supramolecular Polymerization as a Tool to Reveal the Magnetic Transition Dipole Moment of Heptazines, *J. Am. Chem. Soc.*, 2024, **146**, 15843–15849.

48 K. Kogashi, T. Matsuno, S. Sato and H. Isobe, Narrowing Segments of Helical Carbon Nanotubes with Curved Aromatic Panels, *Angew. Chem., Int. Ed.*, 2019, **58**, 7385–7389.

49 Q. Zhou, X. Hou, J. Wang, Y. Ni, W. Fan, Z. Li, X. Wei, K. Li, W. Yuan, Z. Xu, *et al.*, A Fused [5]Helicene Dimer with a Figure-Eight Topology: Synthesis, Chiral Resolution, and Electronic Properties, *Angew. Chem., Int. Ed.*, 2023, **62**, e202302266.

50 T. He, M. Lin, H. Wang, Y. Zhang, H. Chen, C.-L. Sun, Z. Sun, X.-Y. Wang, H.-L. Zhang, Y. Chen, *et al.*, Chiral Cylindrical Molecule with Absorption Dissymmetry Factor Towards Theoretical Limit of 2, *Adv. Theory Simul.*, 2024, **7**, 2300573.

51 J. Nogami, Y. Nagashima, K. Miyamoto, A. Muranaka, M. Uchiyama and K. Tanaka, Asymmetric Synthesis, Structures, and Chiroptical Properties of Helical Cycloparaphenylenes, *Chem. Sci.*, 2021, **12**, 7858–7865.

52 K. Jin, Z. Xiao, H. Xie, X. Shen, J. Wang, X. Chen, Z. Wang, Z. Zhao, K. Yan, Y. Ding, *et al.*, Tether-Entangled Conjugated Helices, *Chem. Sci.*, 2024, **15**, 17128–17149.

53 G. Povie, Y. Segawa, T. Nishihara, Y. Miyauchi and K. Itami, Synthesis of a Carbon Nanobelt, *Science*, 2017, **356**, 172–175.

54 Y. Li, Y. Segawa, A. Yagi and K. Itami, A Nonalternant Aromatic Belt: Methylene-Bridged [6]Cycloparaphenylene Synthesized from Pillar[6]Arene, *J. Am. Chem. Soc.*, 2020, **142**, 12850–12856.

55 G. Povie, Y. Segawa, T. Nishihara, Y. Miyauchi and K. Itami, Synthesis and Size-Dependent Properties of [12], [16], and [24]Carbon Nanobelts, *J. Am. Chem. Soc.*, 2018, **140**, 10054–10059.

56 H. Wang, H. Zhao, S. Chen, L. Bai, Z. Su and Y. Wu, Effective Synthesis of Ladder-type Oligo(*p*-aniline)s and Poly(*p*-aniline)s *via* Intramolecular Snar Reaction, *Org. Lett.*, 2021, **23**, 2217–2221.

57 T. Fukushima, H. Sakamoto, K. Tanaka, Y. Hijikata, S. Irle and K. Itami, Polymorphism of [6]Cycloparaphenylene for Packing Structure-Dependent Host–Guest Interaction, *Chem. Lett.*, 2017, **46**, 855–857.

58 F. Sibbel, K. Matsui, Y. Segawa, A. Studer and K. Itami, Selective Synthesis of [7]- and [8]Cycloparaphenylenes, *Chem. Commun.*, 2014, **50**, 954–956.

59 S. Hitosugi, W. Nakanishi and H. Isobe, Atropisomerism in a Belt-Persistent Nanohoop Molecule: Rotational Restriction Forced by Macrocyclic Ring Strain, *Chem.–Asian J.*, 2012, **7**, 1550–1552.

60 Y. Han, S. Dong, J. Shao, W. Fan and C. Chi, Synthesis of a Sidewall Fragment of a (12,0) Carbon Nanotube, *Angew. Chem., Int. Ed.*, 2021, **60**, 2658–2662.

61 M. Toya, T. Omine, F. Ishiwari, A. Saeki, H. Ito and K. Itami, Expanded [2,1][n]Carbohelicenes with 15- and 17-Benzene Rings, *J. Am. Chem. Soc.*, 2023, **145**, 11553–11565.

62 P. V. R. Schleyer, C. Maerker, A. Dransfeld, H. Jiao and N. J. R. van Eikema Hommes, Nucleus-Independent Chemical Shifts: A Simple and Efficient Aromaticity Probe, *J. Am. Chem. Soc.*, 1996, **118**, 6317–6318.

63 Z. Chen, C. S. Wannere, C. Corminboeuf, R. Puchta and P. V. R. Schleyer, Nucleus-Independent Chemical Shifts (NICS) as an Aromaticity Criterion, *Chem. Rev.*, 2005, **105**, 3842–3888.

64 H. Xie, Z. Xiao, Y. Song, K. Jin, H. Liu, E. Zhou, J. Cao, J. Chen, J. Ding, C. Yi, *et al.*, Tethered Helical Ladder-Type Aromatic Lactams, *J. Am. Chem. Soc.*, 2024, **146**, 11978–11990.

65 L. B. Casabianca, Effect of Curvature on Carbon Chemical Shielding in Extended Carbon Systems, *J. Phys. Chem. A*, 2016, **120**, 7011–7019.

66 T. Iwamoto, Y. Watanabe, Y. Sakamoto, T. Suzuki and S. Yamago, Selective and Random Syntheses of [n]Cycloparaphenylenes (n = 8–13) and Size Dependence of Their Electronic Properties, *J. Am. Chem. Soc.*, 2011, **133**, 8354–8361.

67 H. Kono, Y. Li, R. Zanasi, G. Monaco, F. F. Summa, L. T. Scott, A. Yagi and K. Itami, Methylene-Bridged [6]-, [8]-, and [10]Cycloparaphenylenes: Size-Dependent Properties and Paratropic Belt Currents, *J. Am. Chem. Soc.*, 2023, **145**, 8939–8946.

68 E. R. Darzi, T. J. Sisto and R. Jasti, Selective Syntheses of [7]–[12]Cycloparaphenylenes Using Orthogonal Suzuki–Miyaura Cross-Coupling Reactions, *J. Org. Chem.*, 2012, **77**, 6624–6628.

69 S. Guo, L. Liu, L. Liu, Y. Fan, H. Yang, J. He, Y. Wang, Z. Bo, X. Xu, X. Chen, *et al.*, Naphthalene Diimide-Embedded Donor–Acceptor Carbon Nanohoops: Photophysical, Photoconductive, and Charge Transport Properties, *ACS Appl. Mater. Interfaces*, 2025, **17**, 5202–5212.

70 R. G. Uceda, C. M. Cruz, S. Míguez-Lago, L. Á. de Cienfuegos, G. Longhi, D. A. Pelta, P. Novoa, A. J. Mota, J. M. Cuerva and D. Miguel, Can Magnetic Dipole Transition Moment Be Engineered?, *Angew. Chem., Int. Ed.*, 2024, **63**, e202316696.

71 (*a*) CCDC 2440960: Experimental Crystal Structure Determination, 2025, DOI: **10.5517/ccdc.csd.cc2my0n8**; (*b*) CCDC 2440962: Experimental Crystal Structure Determination, 2025, DOI: **10.5517/ccdc.csd.cc2my0qb**; (*c*) CCDC 2440966: Experimental Crystal Structure Determination, 2025, DOI: **10.5517/ccdc.csd.cc2my0vg**.